Chemical Engineering Journal 509 (2025) 161236

Contents lists available at ScienceDirect

Chemical Engineering Journal

journal homepage: www.elsevier.com/locate/cej

Enhanced built-in electric fields in alkali metal-doped C_3N_5 enable sustainable molecular oxygen activation for water purification

Bin Yang [a,1], Liliang Lu [a,1], Qian Zhang [a], Guixiang Ding [b], Guangfu Liao [b,*], Mei Zhang [a], Xinghuan Liu [a], Raul D. Rodriguez [c,*], Xin Jia [a,*]

[a] School of Chemistry and Chemical Engineering/State Key Laboratory Incubation Base for Green Processing of Chemical Engineering, Shihezi University, Shihezi 832003, PR China
[b] College of Material Engineering, Fujian Agriculture and Forestry University, Fuzhou 350002, PR China
[c] Tomsk Polytechnic University, 30 Lenin Avenue, 634050 Tomsk, Russia

ARTICLE INFO

Keywords:
Photocatalysis
Carbon nitride
Built-in electric fields
Molecular oxygen activation
Water purification

ABSTRACT

The sluggish charge kinetics in photocatalysis is a severely limiting factor for the efficient molecular oxygen for water purification. Here, we report the conversion from amorphous to the crystalline phase of nitrogen-enriched carbon nitride (C_3N_5) via a molten salt strategy, enabling the ordered arrangement of dipole moments and reinforcing spontaneous built-in electric fields that harness directional separation and transfer of photogenerated charges. This unique combination of crystallinity enhancement, defective cyano groups grafting, and interlayer K^+/Na^+ doping synergistically boosts the built-in electric fields and the interlayer shuttling of photogenerated carriers. The interlayered K^+/Na^+–N_3 bridge site in C_3N_5 is able to activate the surface neighboring C and N atoms for boosting the rate-determining step of the photocatalytic molecular oxygen's redox reaction to produce singlet oxygen sustainably. The engineered C_3N_5 demonstrates exceptional degradation activity for various persistent pollutants by releasing singlet oxygen even under harsh environmental conditions. Remarkable, our material displays an unprecedented pollutant removal efficiency with a 100 % degradation rate for up to 15 days of operation with negligible performance attenuation under outdoor sunlight. This successful engineering of the built-in electric field offers a new strategy for organic photocatalysts and the design of advanced materials for efficient and sustainable environmental remediation.

1. Introduction

Reactive oxygen species ($\bullet O_2^-$, $\bullet OH$, $^1O_2$, and H_2O_2) induced via molecular oxygen (O_2) activation have been confirmed to play a crucial role in water purification [1–3]. In recent years, many efforts have been devoted to boosting O_2 activation in photocatalysis [4–6], offering advantages such as being environmentally friendly, simple to operate, inexpensive, and requiring mild reaction conditions. In the photocatalytic O_2 activation, photogenerated electrons combine with O_2 adsorbed on the catalyst surface to form $\bullet O_2^-$, which can be further oxidized or reduced to various reactive oxygen species [7–10]. Polymer metal-free carbon nitride (g-C_3N_4) is a promising photocatalyst for O_2 activation due to its suitable band structure, excellent visible-light response, chemical stability, and simple synthesis method [11–14]. However, the sluggish charge kinetics limits the photocatalytic O_2 activation performance of pristine g-C_3N_4 [15,16]. To overcome these challenges, the strategic engineering of g-C_3N_4 with optimized molecular structures and atomic arrangements to induce spontaneous built-in electric fields (SBEFs) has recently emerged as a promising approach [17,18].

Asymmetric cell structures have a dipole moment derived from delocalized electron cloud distribution [19,20], which generates SBEFs, leading to directional separation and migration of photogenerated charges [21]. Recently, Huang's work reported that g-C_3N_4, composed of heptazine units, possessed in-plane SBEFs due to a uniform distribution of triangular nanopores and a local asymmetric structure [22]. However, according to our density functional theory (DFT) computational results, no dipole moments exist in the highly symmetrical units of g-C_3N_4, implying that this material is not an ideal photocatalyst for generating SBEFs. In addition to the unique advantages of g-C_3N_4, the

* Corresponding authors.
E-mail addresses: liaogf@mail2.sysu.edu.cn (G. Liao), raul@tpu.ru (R.D. Rodriguez), jiaxin@shzu.edu.cn (X. Jia).
[1] These authors contributed equally to this work.

https://doi.org/10.1016/j.cej.2025.161236
Received 12 December 2024; Received in revised form 11 February 2025; Accepted 3 March 2025
Available online 4 March 2025

nitrogen-rich carbon nitride (C_3N_5) photocatalyst is arranged in an asymmetric triazole and triazine framework with a dipole moment of 2.66 D due to charge delocalization [19]. This advantage over g-C_3N_4 allows us to engineer built-in electric fields in C_3N_5 to enhance the behavior of carrier dynamics and further boost photocatalytic performance.

Generally, the C_3N_5 synthesized by traditional methods presents an amorphous structure with plane distortion embodied by activating the n → π* electron transition [23-25]. However, the planar distortion partially cancels the structural units' dipole moments, weakening the SBEFs [26]. Recently, Zhu's group showed that the improved crystallinity of polymer semiconductors could form giant SBEFs and increase the driving force of photogenerated carrier separation and transfer [27,28]. Therefore, transforming C_3N_5 from amorphous to highly crystalline could enable the ordered arrangement of dipole moments, thereby achieving robust SBEFs. Moreover, the molten salt process, with strong mass transfer capacity and appropriate mobility at moderate temperatures, is currently the most viable approach to achieving high crystallization of amorphous organic semiconductors [29,30]. Therefore, we hypothesize that crystallized C_3N_5 could be synthesized via a molten salt strategy, resulting in enhanced SBEFs mediated by ordered dipole moments, supporting an optimized carrier dynamics behavior.

In this context, we have successfully synthesized highly crystalline C_3N_5 rod-shaped aggregates (HCN) with defective cyano group grafting and interlayer alkali K^+/Na^+ doping using a NaCl/KCl molten salts-based process. We found that HCN crystallinity induces a well-ordered arrangement of dipole moments and ensures robust SBEFs for harnessing photogenerated charge separation and directional transfer. The defective cyano group with strong electron extraction increases the structure's polarization rate and electron density, strengthening the SBEFs. The interlayered K^+/Na^+–N_3 bridge site significantly reduces the work function, facilitates interlayer shuttling of photogenerated carriers, and activates the surface neighboring C and N atoms, resulting in the enhanced adsorption and activation of O_2 while boosting the rate-determining step for O_2 to generate singlet oxygen ($^1O_2$) through photocatalytic redox reactions. Sustainably released $^1O_2$ is exploited to degrade various refractory pollutants, including imidacloprid, thiamethoxam, thiacloprid, endinidamine, phenol, and dichlorophenol. Remarkably, our HCN exhibits a remarkable enhancement in the photocatalytic degradation for those pollutants compared to pristine C_3N_5 and maintains 100 % pollutant removal efficiency for up to 15 days of continuous operation under outdoor sunlight. This work offers a new perspective on governing carrier dynamics behaviors and the local electronic environment in organic photocatalysts.

2. Experimental section

2.1. Preparation of C_3N_5 and HCN

C_3N_5 was prepared by thermal polymerization based on Zhang's previous research [24]. About 2.0 g of 3-amino-1,2,4-Triazole powder was placed into a semi-covered ceramic crucible. The crucible is heated to 520 °C at a 5°C/min rate in a muffle furnace, held at 520 °C for 3 h, and then cooled to room temperature.

C_3N_5 (60 mg) was mixed with NaCl (430 mg) and KCl (170 mg) and ground into a uniform solid mixture. The selection of this C_3N_5/NaCl/KCl weight ratio was based on the research of Cheng et al. [37]. The mixture was then calcined at 550 °C in N_2 for 2 h. After natural cooling, the obtained product was washed with 70 °C hot water to remove metal salts. The final sample is recorded as HCN.

2.2. Photocatalytic measurement

The photocatalytic degradation activity of samples was evaluated by the degradation of different pesticides, including imidacloprid, thiamethoxam, thiacloprid, and endinidamine. Specifically, 30 mg catalyst was dispersed in a jacketed beaker containing 50 mL of 10 ppm pesticide aqueous solution under ultrasonication for 10 min. The adsorption–desorption equilibrium was achieved by stirring at room temperature for 30 min. The beaker was maintained at 25 ± 0.5 °C with cooling circulating water and was irradiated at λ ≥ 420 nm visible light using a 300 W Xe lamp (PLS-SXE300D, Beijing Perfectlight Technology Co., Ltd) with a light intensity of 100 mW cm^{-2}. 2 mL of reaction solution was sampled for analysis at intervals of 3 min after removing the photocatalyst through filtration. The pesticide concentration was evaluated using UV-HPLC (Agilent semi preparative HPLC, G1322A, C-18column). In addition, free radical capture experiments were conducted under the same conditions, during which 10 mM of ascorbic acid (LAA), 10 mM of furfuryl alcohol (FFA), 10 mM of triethanolamine (TEOA), and 5 mM of isopropanol (IPA) were added to the solution to capture •O_2^-, $^1O_2$, h^+ and •OH, respectively.

2.3. Continuous flow experiments

The schematic of the custom-made photo-flow device is presented in Fig. S22. The flow reactor was composed of four interconnected quartz tubes 20 cm in length, 1.5 cm in diameter, and 0.1 cm in wall thickness. Each quartz tube was packed with 100 mg of HCN photocatalyst, and both ends consisted of two layers of 4.5 μm filter membrane of 1.5 cm diameter with 0.5 cm thick cotton sandwiched between the filter membrane, thus guaranteeing that the HCN could be stabilized inside the tube without loss. Outdoor sunlight was used to irradiate this reactor, while a peristaltic pump provided a flow rate of 6 ml/h of 10 mg/L IMD solution. The concentration of IMD was measured by taking a liquid every 2 h from 10:00 AM to 8:00 PM in July in Shihezi, Xinjiang. To ensure the even distribution of the catalyst and prevent its deposition at the bottom of the quartz tubes or the filter membranes during the reaction, we controlled the angle between the plate and the ground to be 15 degrees. Additionally, the liquid flow direction in the quartz tube was set from bottom to top. Furthermore, right before the start of each day's experiment, we shook the quartz tubes to disperse the photocatalyst fully.

3. Results and discussion

3.1. Synthesis and characterization of the as-prepared photocatalysts

The synthesis process started from bulk C_3N_5 obtained by the thermal polymerization of 3-amino-1,2,4-Triazole. The crystallized C_3N_5 rod-shaped aggregates (HCN) photocatalyst was further synthesized via a molten salts (NaCl/KCl) process (Fig. 1a). The mixed salts could significantly reduce the melting point of the C_3N_5 precursor and lead to a liquid synthesis [31]. Moreover, the hybrid precursors appeared in a molten state at high temperatures. During the annealing process, C_3N_5 underwent bottom-up three-dimensional (3D) vertical growth on the molten mixture due to the Kirkendall effect caused by the different diffusion rates between the molten salts and C_3N_5. After water washing and desalting, the HCN rod-shaped C_3N_5 aggregates were successfully synthesized.

We confirmed the successful synthesis of C_3N_5 by transmission electron microscopy (TEM) and scanning electron microscopy (SEM) imaging results in Fig. 1b, 1d, and Fig. S1. The electron microscopy results show the amorphous aggregates and the total amorphous region due to plane distortion. As-prepared HCN consisted of well-crystallized rod-shaped aggregates (Fig. 1c, 1e, and Fig. S1b). Moreover, the high-resolution TEM image of HCN in Fig. 1e clearly shows distinct lattice fringes with a spacing of 0.28 nm assigned to the interlayer distance of carbon nitride [32]. In contrast to the selected area electron diffraction (SAED) pattern of C_3N_5, HCN showed a clear single crystal diffraction pattern (Fig. 1d and 1e), evidencing the high crystallinity of the material. In addition, elemental mapping analysis by energy-dispersive X-ray (EDX) spectroscopy showed a uniform distribution of C, N, O, K, and Na

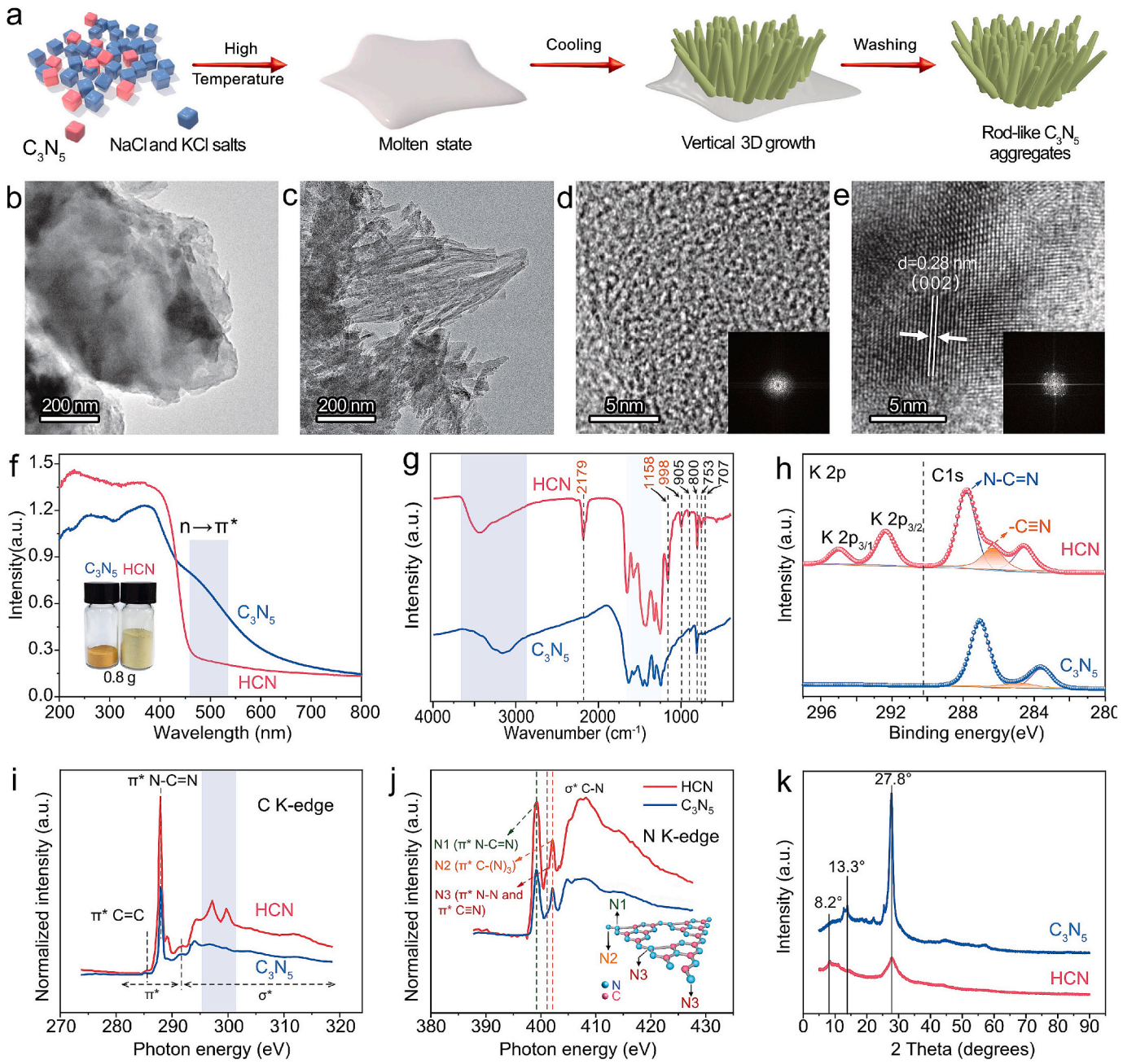

Fig. 1. (a) Schematic illustration of the HCN synthesis route. TEM and HRTEM images of C_3N_5 (b, d) and HCN (c, e). The insets show the SAED patterns of the two samples. (f) UV–Vis DRS spectra, inset is a photograph of samples with the same mass. (g) FTIR spectra. (h) K2p and C1s spectra. C K-edge (i) and N K-edge (j) NEXAFS spectra. (k) XRD patterns.

in HCN (Fig. S1c). These morphological and elemental mapping results confirm our initial hypothesis, demonstrating that molten salts provide a microenvironment for restructuring C_3N_5 from an amorphous distorted plane to a crystalline ordered lattice while successfully introducing K^+ and Na^+ doping.

The crystal structure transformation in C_3N_5 was directly reflected in its optical absorption properties obtained from UV–Vis diffuse reflectance spectroscopy (UV–Vis DRS) (Fig. 1f). The amorphous mediated planar distortion in C_3N_5 results in n–π* electronic transitions, as demonstrated by the strong absorption peak at ~ 490 nm [24]. C_3N_5 also showed an additional absorption edge at ~ 430 nm, attributed to π-π* electron transitions [33]. In contrast, HCN displayed a uniquely extended absorption edge at ~ 470 nm originating from enhanced π-π* electron transitions, and the absorption peak at ~ 490 nm disappeared due to the absence of n–π* transitions. In brief, the UV–Vis DRS analysis suggests that the molten salts process straightened the C_3N_5-distorted plane, matching the observations from HRTEM results.

Organic elemental analysis showed that the N/C ratio of HCN was quite close to C_3N_5 (1.77 vs. 1.67, Fig. S2), indicating that the molten salt process had a less significant effect on the composition and molecular structure. In contrast, the specific surface area of HCN increased to 92.68 cm^2/g compared to 5.30 cm^2/g for C_3N_5 (Fig. S3). This high surface area is attributed to voids left by removing molten salt by water washing, suggesting the creation of an abundance of active sites for catalytic reactions [34]. The Fourier transform infrared (FTIR) spectra of HCN and C_3N_5 have similar characteristics, indicating the preservation of the triazole and triazine frameworks (Fig. 1g) [35]. A clear peak at around 2179 cm^{-1} corresponds to the stretching vibration of cyano

groups. This peak results from the reaction between the molten salt and the triazine moieties during thermal polymerization, which induces the breakage of triazine moieties and the formation of defective cyano groups [36]. In contrast to C_3N_5, there are two new peaks in HCN. One peak at 998 cm^{-1} was indexed to the N-K/Na bonds. Another peak at 1158 cm^{-1} corresponds to the asymmetric vibration of K/Na-NC_2 groups [37], thus revealing that K^+/Na^+ ions were integrated within the HCN interlayer through nitrogen atom coordination between adjacent layers. High-resolution K 2p and Na 1 s X-ray photoelectron spectroscopy (XPS) spectra in Fig. 1h and Fig. S4b directly confirm interlayer alkali K^+/Na^+ doping. Notably, the deconvolution of the C 1 s XPS spectra in HCN yielded two peaks at 287.8 and 284.8 eV (Fig. 1h), corresponding to the binding energy of aromatic N-C=N substances with sp^2-hybridized carbon atoms and graphitic carbon, respectively. Besides, the distinct binding energy peak at 286.3 eV in HCN, originating from defective cyano groups [38], was also consistent with FTIR results.

Near-edge X-ray absorption fine structure (NEXAFS) spectroscopy analysis was performed to probe the samples' local atomic and electronic structure [39,40]. The C K-edge NEXAFS spectra of C_3N_5 and HCN exhibited characteristic excitations, including 1 s → π* out-of-plane C=C at about 285.3 eV and 1 s → π* N-C=N at about 287.9 eV (Fig. 1i). Notably, HCN presented two new characteristic excitations between 295.2 and 301.4 eV, likely associated to interlayer K^+/Na^+ doping [37]. The N K-edge NEXAFS spectra showed similar features for both materials at approximately 399.3, 401.1, and 402.1 eV (Fig. 1j) attributed to 1 s → $\pi^*_{N\text{-}C=N}$, $\pi^*_{heterocyclic\ N\text{-}N}$ of triazole and $\pi^*_{C\text{-}N}$ resonance, respectively. Compared with C_3N_5, HCN had a stronger excitation peak at 401.1 eV due to the introduction of cyano groups into the C_3N_5 framework in the molten salt environment [37]. The X-ray diffraction (XRD) pattern showed two characteristic peaks at 13.3° and 27.8°, corresponding to the in-plane structural ordering (100) and interlayer stacking (002) of C_3N_5, respectively (Fig. 1k) [35,41]. The (002) peak of HCN became weaker and broader, suggesting a reduced interlayer stacking order, possibly due to the larger HCN nanorod size and enhanced condensation and crystallization by the molten salt process that increased mobility. The (100) peak of HCN shifted to a lower diffraction 2θ value (8.2°), indicating an increase in the interlayer stacking distance, attributed to the doping by K^+/Na^+ with larger atomic sizes than carbon and nitrogen. In summary, these results showed that interlayer K^+/Na^+ doping and defective cyano groups were successfully introduced without the influence of the molecular structure of C_3N_5.

3.2. Characterization of SBEFs

The asymmetric triazole and triazine frameworks comprising the amorphous C_3N_5 photocatalyst have dipole moments forming SBEFs. However, dipole moments interacting between the structural units in the distorted plane cancel each other out, resulting in a weakened total SBEFs [42,43]. Notably, the results above showed that the molten salt process can cause the C_3N_5 to change from an amorphous to a crystalline state. This, in turn, causes the distorted planes of the C_3N_5 to straighten and the dipole moments to align constructively, resulting in fully activated SBEFs. To further support this hypothesis, we used theoretical calculations to compare the dipole moments of distorted planes with various structural units and those with flat planes. The calculation results show that the dipole moments were enhanced with the increase in the number of structural units (Fig. 2a and Fig. S5). Meanwhile, the

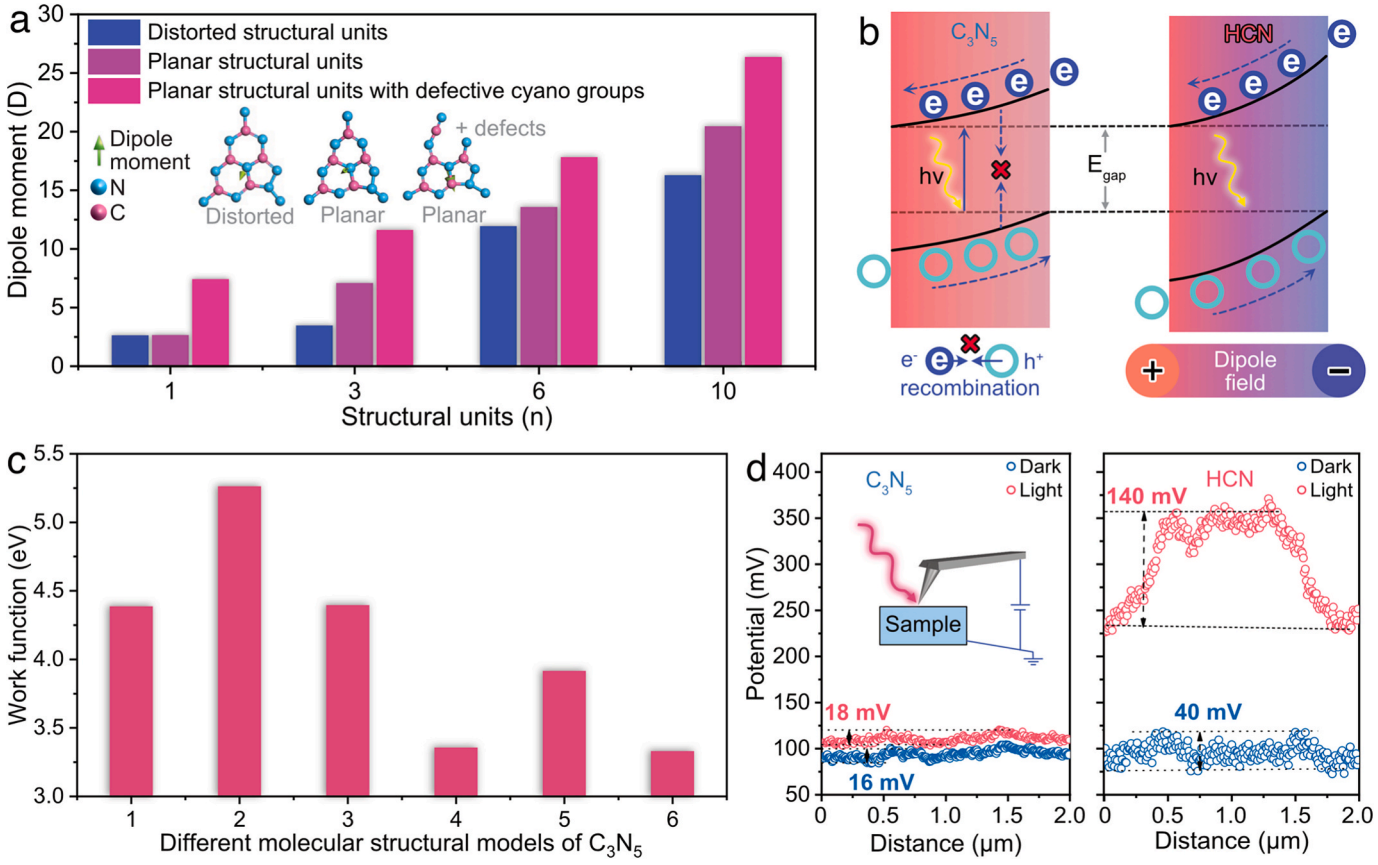

Fig. 2. (a) Dipole moments with different numbers of structural units shown as insets. (b) Schematic of the promotion effect of SBEFs for the separation of photocatalytic charges. (c) Work functions corresponding to different molecular structural models of C_3N_5: 1. Planar C_3N_5; 2. Distorted C_3N_5; 3. Planar C_3N_5 with defective cyano groups; 4. Planar C_3N_5 with interlayer K^+/Na^+ doping; 5. Distorted C_3N_5 with interlayer K^+/Na^+ doping; 6. Planar C_3N_5 with interlayer K^+/Na^+ doping and defective cyano groups. (d) Surface potential cross-sections from KPFM images of C_3N_5 and HCN with and without light irradiation.

dipole moments in the planar structure were stronger than those in the distorted plane. Furthermore, we also investigated how the dipole moments are affected by introducing defective cyano groups into the planar structure (Fig. 2a). The computational results showed that the incorporation of defective cyano groups with strong electron-withdrawing ability further amplified the dipole moments. Based on these results, we investigated the effect of dipole moments on the carriers' kinetic behavior.

Fig. 2b illustrates severe charge recombination due to partial dipole moment offset induced by planar distortions in C_3N_5. This effect results in extremely small energy band bends and weak driving forces for the directional separation of photogenerated charges. Furthermore, when HCN featured a crystalline ordered plane while introducing defective cyano groups, it showed a spatially uneven charge distribution, resulting in strong SBEFs throughout the photocatalyst. The strongly oriented SBEFs could lead to a considerable energy band bending in HCN, promoting charge separation and transfer and further improving photocatalytic activity. In addition, the molten salt process also introduced K^+/Na^+ doping into the C_3N_5 interlayers. The interlayer K^+/Na^+ doping significantly decreases the work function (Fig. 2c), boosting photo-carriers' migration. Interestingly, the work function of interlayer charge transport was also weakened by the straightened plane; however, this effect was not observed when defective cyano groups were introduced. This means that with K^+/Na^+ ions as the migration channels, the photocarriers can quickly shuttle between the straightened layers to reach external catalytic sites, promoting photocatalytic efficiency.

To further gain deeper insights into the surface charge modulation induced by the enhanced SBEFs and interlayer K^+/Na^+ doping, we also explored the surface potential distribution at the surface of C_3N_5 and HCN using Kelvin probe force microscopy (KPFM) combined with a sample light illumination system (Fig. 2d and Fig. S7) [44–46]. In darkness, the surface potential difference between C_3N_5 and HCN with respect to the substrate was 16 and 40 mV, respectively. Under illumination, these values increased to 18 and 140 mV, respectively. The significantly larger change in the surface potential for HCN upon illumination indicates a larger accumulation of photo-generated charges on its surface. The surface potential derived from KPFM is proportional to the built-in electric field [28]. As shown in Fig. S8, the surface potential difference of HCN under illumination outperforms most of the photocatalysts previously reported, indicating its outstanding SBEFs. Consequently, introducing enhanced SBEFs and interlayer alkali K^+/Na^+ doping could significantly enhance the directional migration of photo-generated charges and decrease the transfer resistance between straightened layers. These two processes play a decisive role in the favorable kinetic process of photocatalytic O_2 activation.

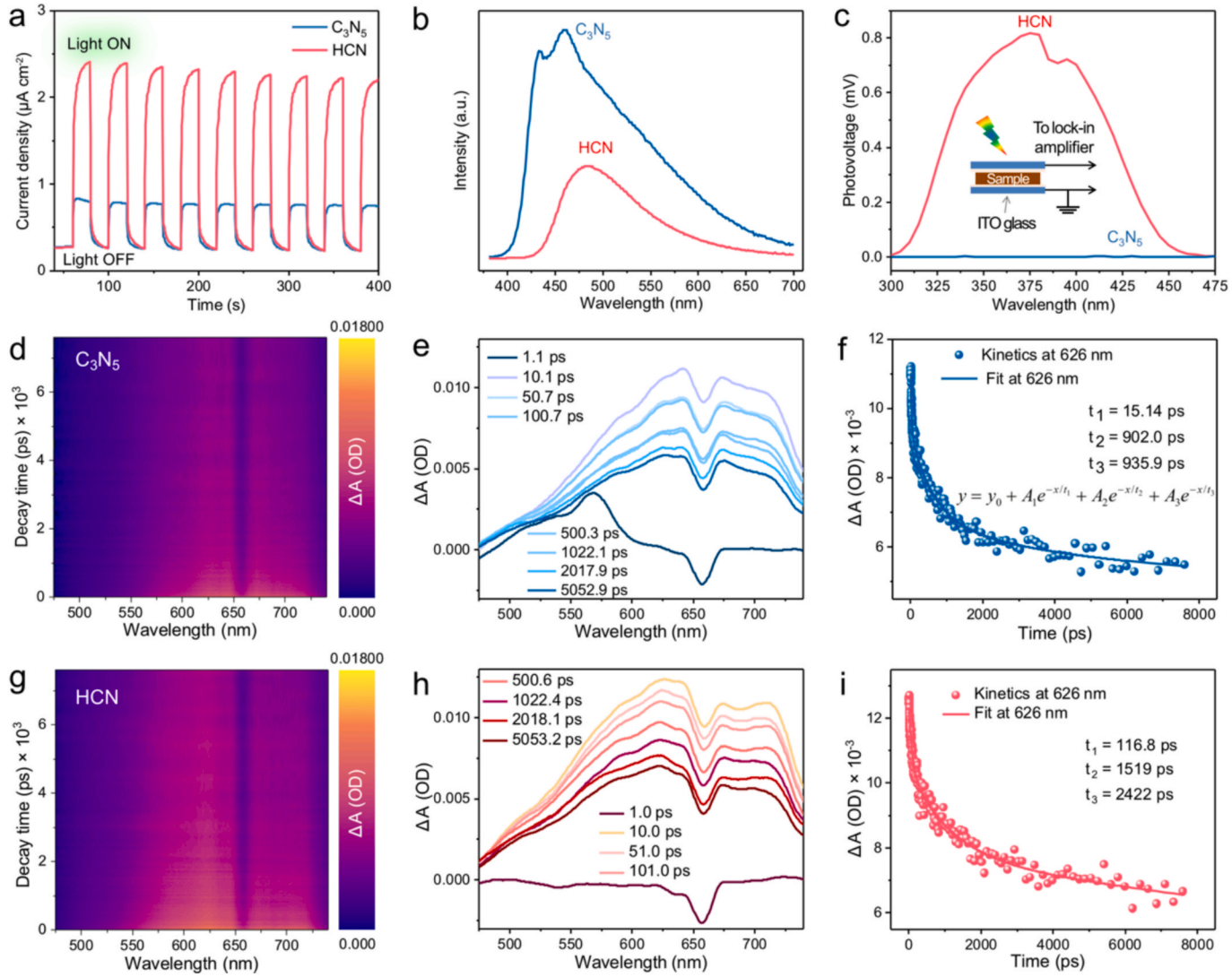

Fig. 3. (a) Photocurrent response, (b) PL, and (c) SPV spectra. 2D pseudo-color maps of fs-TA profile of C_3N_5 (d) and HCN (g), and their corresponding fs-TA spectra at several representative probe delays for C_3N_5 (e) and HCN (h). Kinetics decay profile probed at 626 nm for C_3N_5 (f) and HCN (i).

3.3. Carrier dynamics behavior

To investigate the impact of the enhanced SBEFs and interlayer alkali K^+/Na^+ doping on carrier dynamics, we also used electrochemical impedance spectroscopy (EIS) and photocurrent response to probe the charge transfer resistance and carrier density. We observed a smaller semicircular radius in the EIS Nyquist plot for HCN compared to C_3N_5 (Fig. S9), indicating lower charge transfer resistance in HCN. Furthermore, HCN showed an 8-fold increase in photocurrent density compared to C_3N_5 (Fig. 3a), implying a significantly higher separation efficiency of photogenerated charges. Photoluminescence (PL) results in Fig. 3b show that HCN has a considerably lower PL intensity emission at 482 nm compared to its C_3N_5 counterpart, attributed to inhibited charge recombination due to the intensified SBEFs [47]. Since efficient diffusion of photogenerated carriers to the semiconductor's surface active sites is critical for photocatalysis [48], we further investigated this process by surface photovoltage spectroscopy (SPV) [49]. The SPV signal intensity is correlated with the density of photogenerated charges. As shown in Fig. 3c, HCN presents a remarkable SPV signal in the 300–470 nm, confirming an effective photogenerated charge carrier separation and migration. In contrast, C_3N_5 shows practically no SPV response.

The role of enhanced SBEFs and interlayer alkali K^+/Na^+ doping on the carriers' separation and transport dynamics was further elucidated using femtosecond time-resolved spectroscopy (fs-TAS) analysis [50]. As shown in Fig. 3d and 3e, the negative broad absorption at 440 ~ 580 nm was assigned to the ground state bleach (GSB). The positive broad feature at longer wavelengths was attributed to excited state absorption (ESA) due to trapped photogenerated electrons (e^-) [51]. Notably, HCN had the strongest and longest-lived absorption for ESA compared to its C_3N_5 counterpart. To better understand the relationship between shallow and deep trapping, Fig. 3f and 3i showed the decay kinetics at 626 nm fitted with a tri-exponential function. The time constants (τ_1 and τ_2) represented the recombination of free photogenerated e^- and holes (h^+) and shallow electron trapping, respectively [52,53]. The longer time constant (τ_3) was attributed to unfavorable deep trapping states that deactivated the free e^- and h^+ suppressing photocatalytic efficiency. Notably, HCN with $\tau_1 = 116.8$ ps and $\tau_2 = 1519$ ps exhibited the longest-lived species than C_3N_5 ($\tau_1 = 15$ ps and $\tau_2 = 902$ ps). We attribute this result to free e^- trapped by shallow states, effectively prolonging the

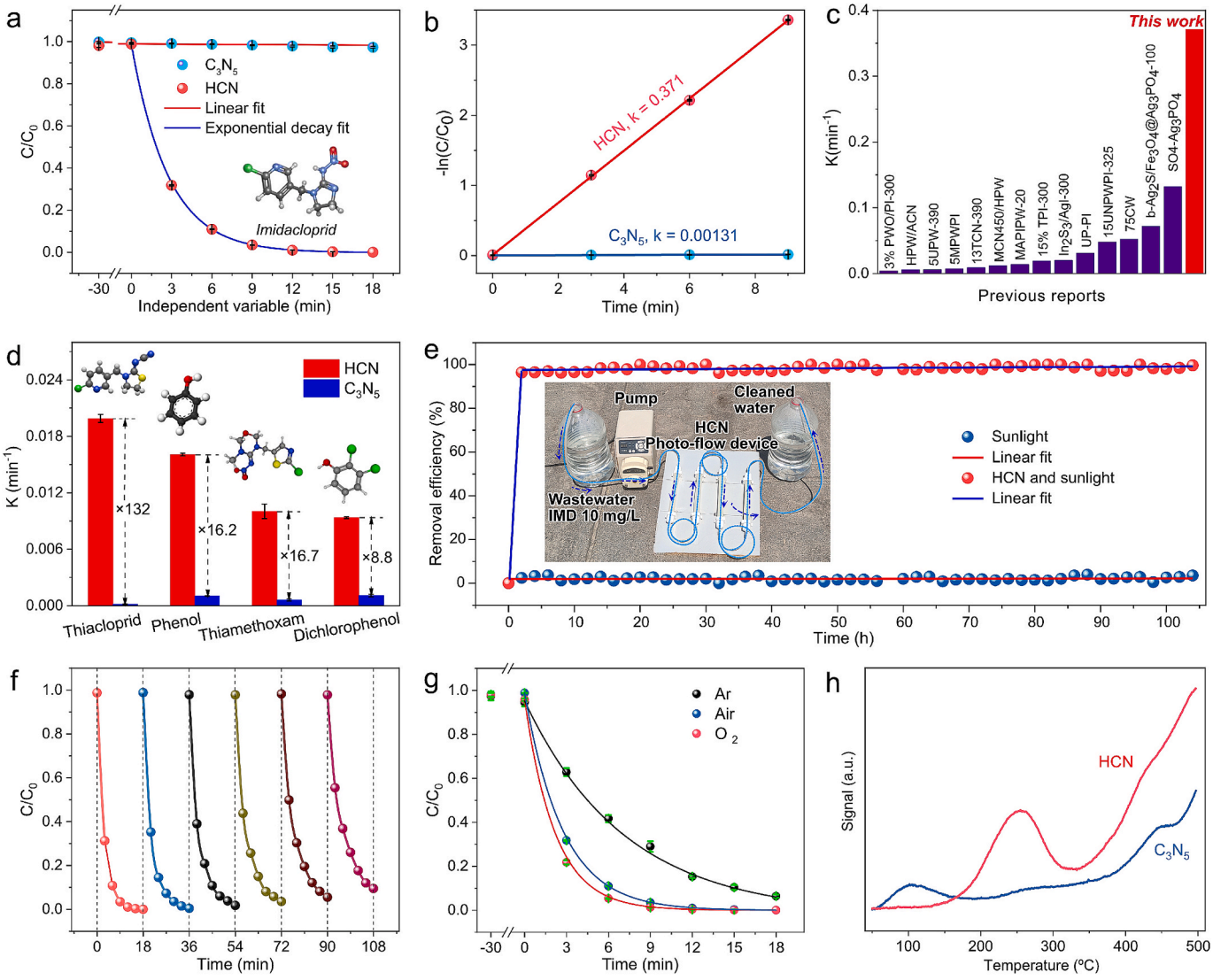

Fig. 4. (a) IMD degradation and (b) the pseudo-first-order kinetic modeling. (c) Comparison performance graph obtained from data in Table S4. (d) Rate constant k for photocatalytic degradation of different pollutants. (e) IMD degradation curves after 15 days of operation in a custom-made photo-flow device under real outdoor sunlight conditions. (f) Cycling stability test of IMD degradation over HTCN in the PC-PMS system. (g) Effect of the dissolved O_2 concentration on the IMD's degradation over HCN. (h) O_2-temperature-programmed desorption profiles.

lifetime of the photogenerated charges [53], which in turn enhances photocatalytic O_2 activation. The fs-TAS results are consistent with the PL, SPV, and photoelectrochemical results discussed above. In other words, the improved carrier migration shows that the enhanced SBEFs and interlayer K^+/Na^+ doping provide a strong driving force and shuttle channels for rapid carrier diffusion to the photocatalyst surface for redox reactions.

3.4. Photocatalytic pollutant degradation

The photocatalytic O_2 activation performance was evaluated using refractory neonicotinoid pesticides, which are widely persistent contaminants in agricultural wastewater, posing a significant risk to water resources and ecosystems [54,55]. The adsorption experiment results in Fig. S10 confirmed negligible imidacloprid (IMD) adsorption on both photocatalysts. Control experiments confirmed IDM's remarkable photostability, showing no signs of degradation under illumination alone without a catalyst. After 12 min of light illumination, C_3N_5 only degraded 2 % of IMD while HCN reached an astonishing 100 % degradation under the same conditions and timeframe (Fig. 4a). Although HCN exhibits lower light absorption above 420 nm compared to C_3N_5, its superior photocatalytic activity is due to its excellent carrier dynamics. The built-in electric fields, interlayer alkali doping, and defective cyano groups collectively enable superior photocatalytic performance. As shown in Fig. 4b, the experimental data were perfectly described by the first-order kinetic equation [$-\ln(C/C_0) = kt$], where C and C_0 were the concentrations at time t and initial concentration at $t = 0$. HCN showed the highest apparent rate constant k of 0.371 min^{-1}, about 280 times higher than that of C_3N_5 (1.31×10^{-3} min^{-1}). We propose a possible degradation pathway of imidacloprid on HCN, illustrated in Fig. S11, revealing a progressive decrease in the intermediates' toxicity. Notably, the intermediate concentration produced by HCN-mediated degradation of IMD decreased with the degradation time, but it is difficult to achieve complete mineralization, while intermediates accumulated for C_3N_5 due to its lower catalytic activity (Fig. S12 and 13). To our knowledge, the photocatalytic degradation of IMD over HCN reported here shows the highest apparent rate constant k among all photocatalysts reported so far (Fig. 4c and Table S4). In addition to IMD, we further demonstrated the exceptional photocatalytic activity of HCN and its broad applicability in the degradation of other neonicotinoid pesticides, including thiamethoxam and thiacloprid, as well as phenol and dichlorophenol, both containing a refractory benzene ring (Fig. 4d and Fig. S14). We specifically selected these compounds due to their widespread occurrence and resistance to conventional removal methods, which make them excellent models for evaluating novel advanced photocatalytic systems' efficiency.

Due to the significance and broad impact of efficient photocatalysts for pollution remediation, we investigated the performance of our HCN material under real-world conditions. For this, we implemented a custom-built continuous photo-flow device depicted in Fig. 4e. The HCN photocatalyst exhibited exceptional stability, still retaining 100 % degradation efficiency of IMD after 15 days of continuous operation at a flow rate of 6 mL h^{-1} under outdoor sunlight. Notably, although the sunlight intensity changes significantly between 10:00 AM and 8:00 PM (Fig. S15), the degradation rate of IMD consistently reaches 100 %. This robust performance is mainly due to the four quartz tubes connected in series, allowing enough light exposure time to degrade IMD completely. We evaluated HCN's performance, demonstrating excellent reusability by retaining 90 % efficiency over six consecutive cycles of IMD degradation (Fig. 4f). FTIR results of HCN before and after IMD degradation experiments confirmed its chemical stability (Fig. S16). Moreover, HCN showed a robust performance under different conditions, including variations in pH, co-existing anions, and different water quality variations (Fig. S17). These results evidenced HCN's potential and competitiveness as a metal-free photocatalyst for the sun-driven degradation of organic pollutants.

3.5. Photocatalytic O_2 activation

To confirm the crucial role of photocatalytic O_2 activation in degrading pollutants, we investigated the effect of O_2 concentration on the catalytic reaction rate. As shown in Fig. 4g and Fig. S18, the degradation rates of IMD over C_3N_5 and HCN were significantly inhibited when the dissolved O_2 concentration was reduced by flowing inert gas through the solution. The degradation rates increased by increasing the dissolved O_2 concentration through continuous O_2 bubbling. These results unequivocally demonstrate that the pollutant degradation is driven by photocatalytic O_2 activation.

The superior O_2 chemisorption ability of HCN was confirmed by temperature-programmed desorption (TPD) results in Fig. 4h [56]. To identify the active species behind this reaction, we performed trapping tests by adding ascorbic acid (LAA), furfuryl alcohol (FFA), isopropanol (IPA), and triethanolamine (TEOA) as quenchers of $\bullet O_2^-$, $^1O_2$, $\bullet OH$, and h^+, respectively [57,58]. The results in Fig. 5a and Fig. S19 showed that adding LAA, FFA, and TEOA significantly compromised the degradation efficiency of imidacloprid (dropping it from 99 % to 8 %, 10 %, and 11 %, respectively). However, adding IPA barely affected the degradation rate (from 99 % to 96.7 %). These observations, combined with the fact that HCN has a valence band (VB) potential of 1.64 V vs. NHE that is not enough to oxidize $OH^-/\bullet OH$ with a standard redox potential of 1.99 V vs. NHE, lead us to conclude that $\bullet O_2^-$, $^1O_2$, and h^+ are the main active species in the photocatalytic degradation of IMD. The generation of these oxygen-containing radicals is a direct consequence of O_2 photocatalytic activation by HCN.

We conducted electron paramagnetic resonance (EPR) analysis to provide direct evidence for the reactive oxygen species (ROS) produced during O_2 photocatalytic activation.[37] Results in Fig. 5b show a significant decrease in TEMPO signal intensity under illumination, confirming the photogeneration of h^+ that reacted and degraded TEMPO. The 1:2:2:1 and 1:1:1:1 peaks in Fig. 5c and Fig. 5d matched with DMPO-$\bullet O_2^-$ and TEMP-$^1O_2$, respectively. These signals were not observed under dark conditions, appearing only under light irradiation. The more significant presence of h^+, $\bullet O_2^-$, and $^1O_2$ in the HCN system than in C_3N_5 perfectly confirms the higher photocatalytic activity of HCN. In Fig. S20, the 1:1:1 DMPO-$\bullet OH$ peak signal was not observed in darkness or under light. The EPR analysis and active species trapping test revealed that $\bullet O_2^-$ and $^1O_2$ are the major ROS components responsible for IMD degradation, while $\bullet OH$ plays no significant role.

3.6. Mechanism of pollutant degradation

Based on the free radical quenching experiments and spectroscopic characterization results, we propose the following photocatalytic O_2 activation mechanism for pollutants degradation on HCN depicted in Fig. 5i, where the band structure was deduced from UV–Vis DRS and XPS valence band spectra (Fig. S21). Visible light irradiation resulted in the photogeneration of e^- and h^+ inside the photocatalyst. The large SBEFs and interlayer K^+/Na^+ doping boosted the separation and directional migration of photogenerated e^- and h^+ to the redox sites, respectively. The conduction band (CB) potential of HCN (-0.67 V vs. NHE) was more negative than the standard redox potential of $O_2/\bullet O_2^-$ (-0.33 V vs. NHE), which implies that e^- migrating to the CB can combine with O_2 to produce $\bullet O_2^-$. There are two main pathways for generating $^1O_2$: energy transfer from the photocatalyst to the triplet ground state of O_2 and photogenerated h^+ oxidation of $\bullet O_2^-$ [58]. Free radical trapping experiments combined with EPR results confirmed that photogenerated h^+ had a dominant effect in the generation of $^1O_2$, supporting the second pathway. The $^1O_2$ produced during this process reacted with pollutant molecules, causing their degradation.

To further demonstrate the superiority of HCN to generate $^1O_2$, in situ diffuse reflectance infrared Fourier transform spectroscopy (DRIFTS) was used to monitor the $\bullet O_2^-$ generated during the reaction [59]. Ethanol was added as an h^+ scavenger to prevent $\bullet O_2^-$ from being

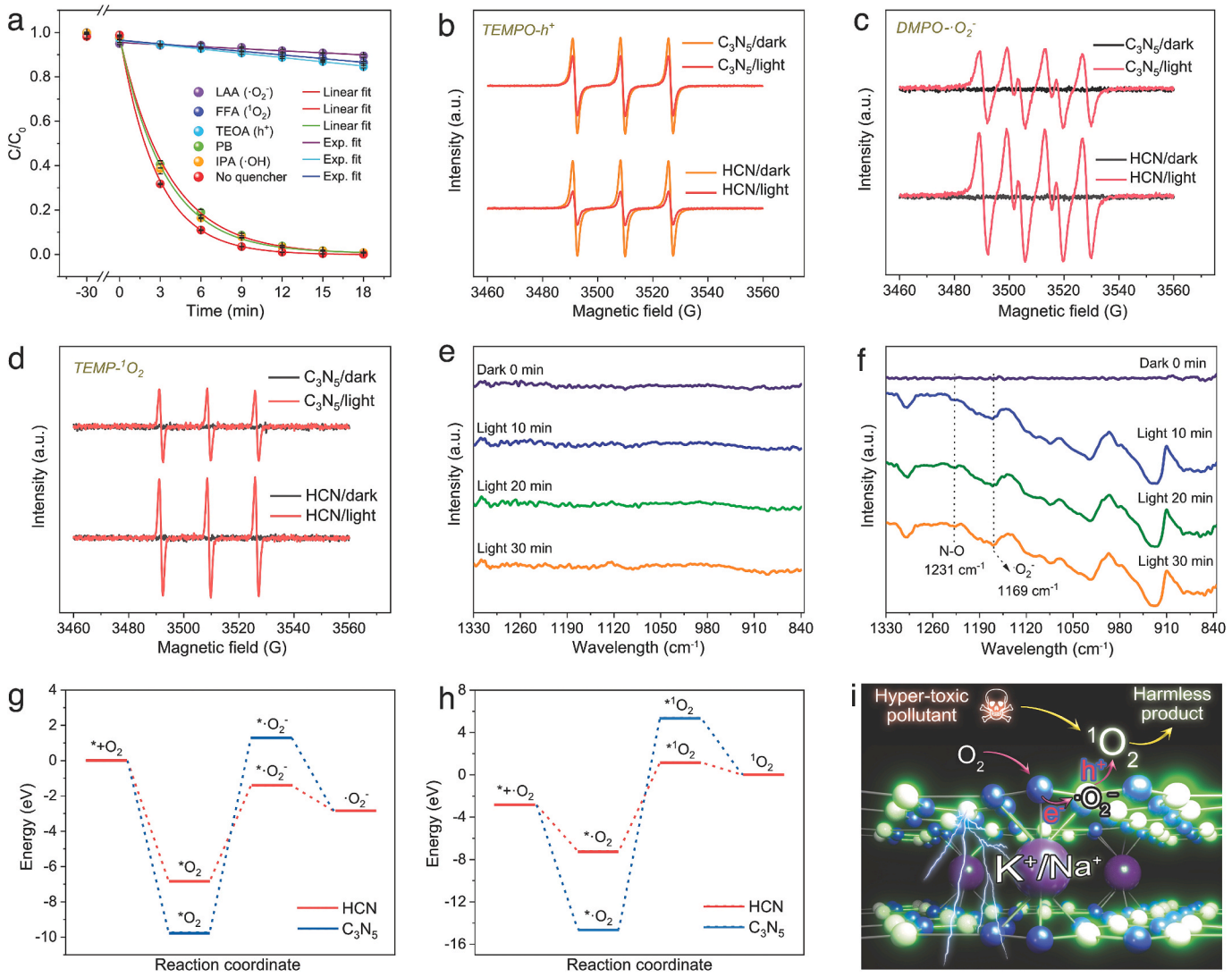

Fig. 5. (a) Impact of different scavengers on IMD degradation over HCN. EPR spectra were recorded for (b) TEMPO-h^+, (c) DMPO-$\bullet O_2^-$, and (d) TEMP-$^1O_2$. In situ DRIFTS spectra of C_3N_5 (e) and HCN (f) in O_2-saturated ethanol and water. ΔG of the O_2 reduction to $\bullet O_2^-$ by photogenerated e^- (g) and ΔG of the $\bullet O_2^-$ oxidation to $^1O_2$ by photogenerated h^+ (h) over TCN and HTCN, respectively. (i) Proposed mechanism of photocatalytic O_2 activation for pollutants' degradation.

further oxidized to $^1O_2$ by photogenerated h^+. While C_3N_5 did not show apparent peaks under dark or light illumination conditions (Fig. 5e), as well as HCN in the dark, peaks at 1231 cm^{-1} and 1168 cm^{-1} appeared under visible light illumination of HCN (Fig. 5f). These peaks attributed to N-O and $\bullet O_2^-$, suggested that photoactivated HCN facilitated O_2 adsorption at its N active sites as the reduction center, and then generated the intermediate $\bullet O_2^-$ species towards $^1O_2$ transformation.

DFT calculations were performed to gain further insights into the favorable formation pathway of $^1O_2$ on HCN. DFT calculations' results of intermediate species, transition states, and the corresponding Gibbs free energies (ΔG) were obtained at each step of $\bullet O_2^-$ and $^1O_2$ evolution by O_2 redox reactions on the surface of HCN and C_3N_5. The neighboring N and C atoms near K^+/Na^+ anions were selected as the primary reduction and oxidation active sites, respectively. As shown in Fig. 5g and 5 h, the ΔG of HCN for N-O_2 reduced to N-$\bullet O_2^-$ and C-$\bullet O_2^-$ oxidized to C-$^1O_2$ were increased by 5.4 and 8.8 eV, respectively, indicating a more favorable conversion on the HCN surface than C_3N_5 counterpart. These results explain the faster reaction rate experimentally observed for the O_2 conversion to $^1O_2$ catalyzed by HCN and its significantly superior performance over C_3N_5.

In short, this work features several novelty points: 1) The synergistic enhancement of SBEFs in C_3N_5 by both the crystallization and the introduction of defective cyano groups. 2) The dual role of interlayer K^+/Na^+ doping in promoting carrier migration and activating surface C and N atoms. 3) Our engineered HCN demonstrates extraordinary degradation activity for various pollutants by generating and releasing $^1O_2$ through photocatalytic O_2 activation. Moreover, our material achieves near 100 % pollutant degradation efficiency under different scenarios, including in a continuous photo-flow device for up to 15 days with negligible performance attenuation under real outdoor sunlight conditions.

4. Conclusion

In summary, we successfully synthesized highly crystalline rod-shaped C_3N_5 aggregates with defective cyano groups grafting and interlayer alkali K^+/Na^+ doping via molten salt. This unique structural configuration significantly boosts the $^1O_2$ generation through photocatalytic O_2 activation, resulting in 100 % IMD degradation within 12 min with a superior reaction rate constant K (0.371 min^{-1}). This material shows exceptional stability, retaining 100 % degradation efficiency for pollutants in water under sunlight for 15 days; remarkably, the system achieved complete removal degradation at all times, even despite varying sunlight intensity during the day. We systematically

analyzed the entire photocatalytic O_2 activation process, experimentally and theoretically, revealing that the enhanced SBEFs are formed by structural characteristics of the orderly arrangement of dipole moments and the introduced defective cyano groups. Simultaneously, the interlayered K^+/Na^+–N_3 bridge site promotes interlayer carrier migration by significantly reducing the work function and activates the surface neighboring C and N atoms to boost the rate-determining step of the photocatalytic O_2's redox reaction. The unique HCN structural configuration improves charge separation efficiency, promotes O_2 chemisorption, and enhances O_2 conversion to $^1O_2$ through redox reaction, thereby significantly boosting photocatalytic O_2 activation for the efficient degradation of various pollutants, including refractory neonicotinoid pesticides, phenol, and dichlorophenol. This work provides a new reference for engineering the SBEFs of metal-free photo(electro) catalytic materials for solar-light-driven O_2 activation, pushing our way toward sustainable environmental remediation and beyond.

CRediT authorship contribution statement

Bin Yang: Writing – review & editing, Writing – original draft, Visualization, Validation, Supervision, Software, Resources, Project administration, Methodology, Investigation, Funding acquisition, Formal analysis, Data curation, Conceptualization. **Liliang Lu:** Project administration, Methodology, Data curation. **Qian Zhang:** Writing – review & editing, Writing – original draft, Conceptualization. **Guixiang Ding:** Software. **Guangfu Liao:** Writing – original draft. **Mei Zhang:** Formal analysis. **Xinghuan Liu:** Formal analysis. **Raul D. Rodriguez:** Writing – review & editing, Writing – original draft. **Xin Jia:** Writing – review & editing, Supervision, Resources, Funding acquisition.

Declaration of competing interest

The authors declare that they have no known competing financial interests or personal relationships that could have appeared to influence the work reported in this paper.

Acknowledgments

This study was mainly supported by the National Natural Science Foundation of China (Grant No. 22308223), the High-level Talents launching Project (RCZK202328), and Xinjiang Uygur Autonomous Region Tianchi Talent Introduction Program (Young Doctor) for Bin Yang. This study was also supported by the National Natural Science Foundation of China (Grant No. U1703351, 52073179), Tiansh a Talent Support Program for Xin Jia, and the Program of Introducing Talents of Discipline to Universities (D20018). RDR acknowledges the Agrochemical Engineering Innovation and Intelligence Base for Oasis Ecology.

Appendix A. Supplementary data

Supplementary data to this article can be found online at https://doi.org/10.1016/j.cej.2025.161236.

Data availability

Data will be made available on request.

References

[1] H. Qin, M. Guo, C. Zhou, J. Li, X. Jing, Y. Wan, W. Song, H. Yu, G. Peng, Z. Yao, J. Liu, K. Hu, Enhancing singlet oxygen production of dioxygen activation on the carbon-supported rare-earth oxide nanocluster and rare-earth single atom catalyst to remove antibiotics, Water Res. 252 (2024) 121184.
[2] Y. Tao, Y. Hou, H. Yang, Z. Gong, J. Yu, H. Zhong, Q. Fu, J. Wang, F. Zhu, G. Ouyang, Interlayer synergistic reaction of radical precursors for ultraefficient $^1O_2$ generation via quinone-based covalent organic framework, Proc. Natl. Acad. Sci. USA 121 (2024) e2401175121.
[3] S. Wang, Z. Xiong, N. Yang, X. Ding, H. Chen, Iodine-doping-assisted tunable introduction of oxygen vacancies on bismuth tungstate photocatalysts for highly efficient molecular oxygen activation and pentachlorophenol mineralization, Chin. J. Catal. 41 (2022) 1544–1553.
[4] Y. Qian, D. Li, Y. Han, H.-L. Jiang, Photocatalytic molecular oxygen activation by regulating excitonic effects in covalent organic frameworks, J. Am. Chem. Soc. 142 (2020) 20763–20771.
[5] F. Guo, C. Mao, C. Liang, P. Xing, L. Yu, Y. Shi, S. Cao, F. Wang, X. Liu, Z. Ai, L. Zhang, Triangle Cl-Ag_1-Cl sites for superior photocatalytic molecular oxygen activation and NO oxidation of BiOCl, Angew. Chem. Int. Ed. 62 (2023) e202314243.
[6] S. Suleman, Y. Zhang, Y. Qian, J. Zhang, Z. Lin, Ö. Metin, Z. Meng, H.-L. Jiang, Turning on singlet oxygen generation by outer-sphere microenvironment modulation in porphyrinic covalent organic frameworks for photocatalytic oxidation, Angew. Chem. Int. Ed. 63 (2024) e202314988.
[7] R. Banyal, A. Sudhaik, R. Kumar, P. Sonu, T. Raizada, S. Ahamad, M.M. Kaya, V. Maslov, C.M. Chaudhary, P.S. Hussain, Construction of novel BiOI/$CuInS_2$/ZnO Dual S-scheme charge transfer pathway for efficient antibiotic degradation, J. Phys. Chem. Solids 195 (2024) 112132.
[8] V. Soni, A. Sonu, P. Sudhaik, S. Singh, T. Thakur, V. Ahamad, L.P. Nguyen, H.H. P. Thi, V. Quang, P.R. Chaudhary, Visible-light-driven photodegradation of methylene blue and doxycycline hydrochloride by waste-based S-scheme heterojunction photocatalyst Bi_5O_7I/PCN/tea waste biochar, Chemosphere 347 (2024) 140694.
[9] V. Dutta, P. Sonu, P.K. Raizada, T. Verma, S. Ahamad, C.M. Thakur, P.S. Hussain, Constructing carbon nanotubes@$CuBi_2O_4$/$AgBiO_3$ all solid-state mediated Z-scheme photocatalyst with enhanced photocatalytic activity, Mater. Lett. 320 (2022) 132374.
[10] K. Singh, S. Abhimanyu, V. Sonu, P. Chaudhary, S. Raizada, P. Rustagi, P. Singh, V. Thakur, A.K. Kumar, Defect and Heterostructure engineering assisted S-scheme Nb_2O_5 nanosystems-based solutions for environmental pollution and energy conversion, Adv. Colloid Interface Sci. 332 (2024) 103273.
[11] J. Zhang, L. Pan, X. Zhang, C. Shi, J. Zou, Donor-acceptor carbon nitride with electron-withdrawing chlorine group to promote exciton dissociation, Chin. J. Catal. 42 (2021) 1168–1175.
[12] S. Feng, X. Li, P. Kong, X. Gu, Y. Wang, N. Wang, R. Hailili, Z. Zheng, Regulation of the tertiary N site by edge activation with an optimized evolution path of the hydroxyl radical for photocatalytic oxidation, ACS Catal. 13 (2023) 8708–8719.
[13] G. Liao, Y. Gong, L. Zhang, H. Gao, G.-J. Yang, B. Fang, Semiconductor polymeric graphitic carbon nitride photocatalysts: the "holy grail" for the photocatalytic hydrogen evolution reaction under visible light, Energy Environ. Sci. 12 (2019) 2080–2147.
[14] B. Liu, J. Du, G. Ke, B. Jia, Y. Huang, H. He, Y. Zhou, Z. Zou, Boosting O_2 reduction and H_2O dehydrogenation kinetics: surface N-hydroxymethylation of g-C_3N_4 photocatalysts for the efficient production of H_2O_2, Adv. Funct. Mater. 32 (2022) 2111125.
[15] D. Zhao, Y. Wang, C.-L. Dong, Y.-C. Huang, J. Chen, F. Xue, S. Shen, L. Guo, Boron-doped nitrogen-deficient carbon nitride-based Z-scheme heterostructures for photocatalytic overall water splitting, Nat. Energy 6 (2021) 388–397.
[16] B. Yang, X. Li, Q. Zhang, X. Yang, J. Wan, G. Liao, J. Zhao, R. Wang, J. Liu, R. D. Rodriguez, X. Jia, Ultrathin porous carbon nitride nanosheets with well-tuned band structures via carbon vacancies and oxygen doping for significantly boosting H_2 production, Appl. Catal. B Environ. Energy 314 (2022) 121521.
[17] W. Zeng, Y. Dong, X. Ye, Z. Zhang, T. Zhang, X. Guan, L. Guo, Crystalline carbon nitride with in-plane SBEFs accelerates carrier separation for excellent photocatalytic hydrogen evolution, Chin. Chem. Lett. 35 (2024) 109252.
[18] B. Yan, C. Du, G. Yang, Constructing SBEFs in ultrathin graphitic carbon nitride nanosheets by N and O codoping for enhanced photocatalytic hydrogen evolution activity, Small 16 (2020) 1905700.
[19] J. Li, Q. Chai, R. Niu, W. Pan, Z. Chen, L. Wang, K. Wang, Z. Liu, Y. Liu, Y. Xiao, B. Liu, Identification of intrinsic vacancies and polarization effect on ternary halo-sulfur-bismuth compounds for efficient CO_2 photoreduction under near-infrared light irradiation, Carbon Energy 4 (2024) e598.
[20] X. Zhu, Y. Jia, Y. Liu, J. Xu, H. He, S. Wang, Y. Shao, Y. Zhai, Y. Zhu, Enhancing SBEFs via molecular symmetry modulation in supramolecular photocatalysts for highly efficient photocatalytic hydrogen evolution, Angew. Chem. Int. Ed. 63 (2024) e202405962.
[21] T. Lv, J. Li, N. Arif, L. Qi, J. Lu, Z. Ye, Y. Zeng, Polarization and external-field enhanced photocatalysis, Matter 5 (2022) 2685–2721.
[22] C. Hu, F. Chen, Y. Wang, N. Tian, T. Ma, Y. Zhang, H. Huang, Exceptional cocatalyst-free photo-enhanced piezocatalytic hydrogen evolution of carbon nitride nanosheets from strong in-plane polarization, Adv. Mater. 33 (2021) 2101751.
[23] C. Peng, L. Han, J. Huang, S. Wang, X. Zhang, H. Chen, Comprehensive investigation on robust photocatalytic hydrogen production over C_3N_5, Chin. J. Catal. 43 (2022) 410–420.
[24] Y. Tong, S. Huang, X. Zhao, Y. Yang, L. Feng, Q. Han, L. Zhang, Peroxymonosulfate activation by boron doped C_3N_5 metal-free materials with n → π* electronic transitions for tetracycline degradation under visible light: insights into the generation of reactive species, Chem. Eng. J. 480 (2024) 147693.
[25] S. Hu, D. Jiang, L. Gu, G. Xu, Z. Li, Y. Yuan, Awakening n→π* electronic transition by breaking hydrogen bonds in graphitic carbon nitride for increased photocatalytic hydrogen generation, Chem. Eng. J. 399 (2020) 125847.

[26] X. Yue, J. Fan, Q. Xiang, Internal electric field on steering charge migration: modulations, determinations and energy-related applications, Adv. Funct. Mater. 32 (2022) 2110258.
[27] Z. Zhang, X. Chen, H. Zhang, W. Liu, W. Zhu, Y. Zhu, A highly crystalline perylene imide polymer with the robust SBEFs for efficient photocatalytic water oxidation, Adv. Mater. 32 (2020) 1907746.
[28] X. Xu, L. Meng, J. Zhang, S. Yang, C. Sun, H. Li, J. Li, Y. Zhu, Full-spectrum responsive naphthalimide/perylene diimide with a giant internal electric field for photocatalytic overall water splitting, Angew. Chem. Int. Ed. 63 (2024) e202308597.
[29] H. Ou, L. Lin, Y. Zheng, P. Yang, Y. Fang, X. Wang, Tri-*s*-triazine-based crystalline carbon nitride nanosheets for an improved hydrogen evolution, Adv. Mater. 29 (2017) 1700008.
[30] L. Wang, L. Liu, Y. Li, Y. Xu, W. Nie, Z. Cheng, Q. Zhou, L. Wang, Z. Fan, Molecular-level regulation strategies toward efficient charge separation in donor−acceptor type conjugated polymers for boosted energy-related photocatalysis, Adv. Energy Mater. 14 (2024) 2303346.
[31] H. Jin, Q. Gu, B. Chen, C. Tang, Y. Zheng, H. Zhang, M. Jaroniec, S.-Z. Qiao, Molten salt-directed catalytic synthesis of 2D layered transition-metal nitrides for efficient hydrogen evolution, Chem 6 (2020) 2382–2394.
[32] F. He, Y. Lu, Y. Wu, S. Wang, Y. Zhang, P. Dong, Y. Wang, C. Zhao, S. Wang, J. Zhang, S. Wang, Rejoint of carbon nitride fragments into multi-interfacial order-disorder homojunction for robust photo-driven generation of H_2O_2, Adv. Mater. 36 (2024) 2307490.
[33] P. Kumar, G. Singh, X. Guan, J. Lee, R. Bahadur, K. Ramadass, P. Kumar, M. G. Kibria, D. Vidyasagar, J. Yi, A. Vinu, Multifunctional carbon nitride nanoarchitectures for catalysis, Chem. Soc. Rev. 52 (2023) 7602–7664.
[34] X. Liu, A. Ronne, L.-C. Yu, Y. Liu, M. Ge, C.-H. Lin, B. Layne, P. Halstenberg, D. S. Maltsev, A.S. Ivanov, S. Antonelli, S. Dai, W.-K. Lee, S.M. Mahurin, A.I. Frenkel, J.F. Wishart, X. Xiao, Formation of three-dimensional bicontinuous structures via molten salt dealloying studied in real-time by in situ synchrotron X-ray nano-tomography, Nat. Commun. 12 (2021) 3441.
[35] C. Fu, T. Wu, G. Sun, G. Yin, C. Wang, G. Ran, Q. Song, Dual-defect enhanced piezocatalytic performance of C_3N_5 for multifunctional applications, Appl. Catal. B Environ. Energy 323 (2023) 122196.
[36] Y. Li, Y. Xue, X. Gao, L. Wang, X. Liu, Z. Wang, S. Shen, Cayanamide group functionalized crystalline carbon nitride aerogel for efficient CO_2 photoreduction, Adv. Funct. Mater. 34 (2024) 2312634.
[37] C. Cheng, L. Mao, X. Kang, C.-L. Dong, Y.-C. Huang, S. Shen, J. Shi, L. Guo, A high-cyano groups-content amorphous-crystalline carbon nitride isotype heterojunction photocatalyst for high-quantum-yield H_2 production and enhanced CO_2 reduction, Appl. Catal. B Environ. Energy 331 (2023) 122733.
[38] E. Hu, Q. Chen, Q. Gao, X. Fan, X. Luo, Y. Wei, G. Wu, H. Deng, S. Xu, P. Wang, L. Liu, R. He, X. Chen, W. Zhu, Y. Zhu, Cyano-functionalized graphitic carbon nitride with adsorption and photoreduction isosite achieving efficient uranium extraction from seawater, Adv. Funct. Mater. 34 (2024) 2312215.
[39] G. Liao, L. Zhang, C. Li, S.-Y. Liu, B. Fang, H. Yang, Emerging carbon-supported single-atom catalysts for biomedical applications, Matter 5 (2022) 3341–3374.
[40] T.M. Ajayi, N. Shirato, T. Rojas, S. Wieghold, X. Cheng, K.Z. Latt, D.J. Trainer, N. K. Dandu, Y. Li, S. Premarathna, S. Sarkar, D. Rosenmann, Y. Liu, N. Kyritsakas, S. Wang, E. Masson, V. Rose, X. Li, A.T. Ngo, S.-W. Hla, Characterization of just one atom using synchrotron X-rays, Nature 618 (2023) 69–73.
[41] C. Fu, M. Zhao, X. Chen, G. Sun, C. Wang, Q. Song, Unraveling the dual defect effects in C3N5 for piezo-photocatalytic degradation and H_2O_2 generation, Appl. Catal. B Environ. Energy 332 (2023) 122752.
[42] J. Pillardy, R.J. Wawak, Y.A. Arnautova, C. Czaplewski, H.A. Scheraga, Crystal structure prediction by global optimization as a tool for evaluating potentials: role of the dipole moment correction term in successful predictions, J. Am. Chem. Soc. 122 (2000) 907–921.
[43] K.D. Jordan, F. Wang, Theory of dipole-bound anions, Chem. Soc. Rev. 54 (2003) 367–396.
[44] H. Zhu, L. Gou, C. Li, X. Fu, Y. Weng, L. Chen, B. Fang, L. Shuai, G. Liao, Dual interfacial electric fields in black phosphorus/MXene/MBene enhance broad-spectrum carrier migration efficiency of photocatalytic devices, Device 2 (2024) 100283.
[45] M. Checa, A.S. Fuhr, C. Sun, R. Vasudevan, M. Ziatdinov, I. Ivanov, S.J. Yun, K. Xiao, A. Sehirlioglu, Y. Kim, P. Sharma, K.P. Kelley, N. Domingo, S. Jesse, L. Collins, High-speed mapping of surface charge dynamics using sparse scanning Kelvin probe force microscopy, Nat. Commun. 14 (2023) 7196.
[46] R. Chen, Z. Ren, Y. Liang, G. Zhang, T. Dittrich, R. Liu, Y. Liu, Y. Zhao, S. Pang, H. An, C. Ni, P. Zhou, K. Han, F. Fan, C. Li, Spatiotemporal imaging of charge transfer in photocatalyst particles, Nature 610 (2022) 296–301.
[47] J.S. Bangsund, J.R. Van Sambeek, N.M. Concannon, R.J. Holmes, Sub-turn-on exciton quenching due to molecular orientation and polarization in organic light-emitting devices, Sci. Adv. 6 (2020) eabb2659.
[48] B. Yang, J. Zhao, Y. Xiong, C. Li, M. Zhang, R.D. Rodriguez, X. Jia, Vacancies engineering in ultrathin porous g-C_3N_4 tubes for enhanced photocatalytic PMS activation for imidacloprid degradation, Chem. Eng. J. 298 (2024) 155117.
[49] Y. Zhang, C. Pan, G. Bian, J. Xu, Y. Dong, Y. Zhang, Y. Lou, W. Liu, Y. Zhu, H_2O_2 generation from O_2 and H_2O on a near-infrared absorbing porphyrin supramolecular photocatalyst, Nat. Energy 8 (2023) 361–371.
[50] J. Zhang, B. Zhu, L. Zhang, J. Yu, Femtosecond transient absorption spectroscopy investigation into the electron transfer mechanism in photocatalysis, Chem. Commun. 59 (2023) 688–699.
[51] R. Godin, Y. Wang, M.A. Zwijnenburg, J. Tang, J.R. Durrant, Time-resolved spectroscopic investigation of charge trapping in carbon nitrides photocatalysts for hydrogen generation, J. Am. Chem. Soc. 139 (2017) 5216–5224.
[52] J. Ma, T.J. Miao, J. Tang, Charge carrier dynamics and reaction intermediates in heterogeneous photocatalysis by time-resolved spectroscopies, Chem. Soc. Rev. 51 (2022) 5777–5794.
[53] Y. Zhang, Q. Cao, A. Meng, X. Wu, Y. Xiao, C. Su, Q. Zhang, Molecular heptazine-triazine junction over carbon nitride frameworks for artificial photosynthesis of hydrogen peroxide, Adv. Mater. 35 (2023) 2306831.
[54] K. Yin, Y. Deng, C. Liu, Q. He, Y. Wei, S. Chen, T. Liu, S. Luo, Kinetics, pathways and toxicity evaluation of neonicotinoid insecticides degradation via UV/chlorine process, Chem. Eng. J. 346 (2018) 298–306.
[55] X. Wang, D. Goulson, L. Chen, J. Zhang, W. Zhao, Y. Jin, S. Yang, Y. Li, J. Zhou, Occurrence of neonicotinoids in chinese apiculture and a corresponding risk exposure assessment, Environ. Sci. Technol. 54 (2020) 5021–5030.
[56] Y. Hou, P. Zhou, F. Liu, K. Tong, Y. Lu, Z. Li, J. Liang, M. Tong, Rigid covalent organic frameworks with thiazole linkage to boost oxygen activation for photocatalytic water purification, Nat. Commun. 15 (2024) 7350.
[57] Y. Yang, C. Zhang, D. Huang, G. Zeng, J. Huang, C. Lai, C. Zhou, W. Wang, H. Guo, W. Xue, R. Deng, M. Cheng, W. Xiong, Boron nitride quantum dots decorated ultrathin porous g-C_3N_4: Intensified exciton dissociation and charge transfer for promoting visible-light-driven molecular oxygen activation, Appl. Catal. B Environ. Energy 245 (2019) 87–99.
[58] M. Xu, R. Wang, H. Fu, Y. Shi, L. Ling, Harmonizing the cyano-group and Na to enhance selective photocatalytic O_2 activation on carbon nitride for refractory pollutant degradation, Proc. Natl. Acad. Sci. USA 121 (2024) e2318787121.
[59] F. Hao, C. Yang, X. Lv, F. Chen, S. Wang, G. Zheng, Q. Han, Photo-driven quasi-topological transformation exposing highly active nitrogen cation sites for enhanced photocatalytic H_2O_2 production, Angew. Chem. Int. Ed. 62 (2023) e202315456.